Journal of the Optical Society of America B
OPTICAL PHYSICS

Retrieval of the complex-valued refractive index of germanium near the $M_{4,5}$ absorption edge

Christopher J. Kaplan,[1] Peter M. Kraus,[1,6] Eric M. Gullikson,[2] L. J. Borja,[1] Scott K. Cushing,[5] Michael Zürch,[1,7] Hung-Tzu Chang,[1] Daniel M. Neumark,[1,3] and Stephen R. Leone[1,3,4,*]

[1]Department of Chemistry, University of California, Berkeley, California 94720, USA
[2]Center for X-ray Optics, Lawrence Berkeley National Laboratory, Berkeley, California 94720, USA
[3]Chemical Sciences Division, Lawrence Berkeley National Laboratory, Berkeley, California 94720, USA
[4]Department of Physics, University of California, Berkeley, California 94720, USA
[5]Current address: Department of Chemistry, California Institute of Technology, Pasadena, California 91125, USA
[6]Current address: Advanced Research Center for Nanolithography, Science Park 106, 1098 XG Amsterdam, The Netherlands
[7]Current address: Fritz Haber Institute of the Max Planck Society, Department of Physical Chemistry, Berlin, Germany
*Corresponding author: srl@berkeley.edu

Received 22 March 2019; revised 23 April 2019; accepted 24 April 2019; posted 25 April 2019 (Doc. ID 362900); published 31 May 2019

The complex-valued index of refraction of germanium in the extreme ultraviolet (XUV) is measured by multi-angle reflectance of synchrotron radiation. The resulting index of refraction is higher resolution than previously measured values. It reveals new structures attributed to transitions from the 3d-core orbitals to the $\Sigma^c_{5,2}$ and the $X^c_{5,2}$ conduction bands. Additionally, it is shown that the problem of total external reflection, which renders multi-angle reflectance measurements insensitive to the complex-valued refractive index at grazing incidence, can be overcome by employing measurements at angles of incidence away from the critical angle.

https://doi.org/10.1364/JOSAB.36.001716

1. INTRODUCTION

The complex refractive index describes the linear optical properties of a material, directly providing the reflection of light from a surface and the absorptivity of the material [1]. The refractive index is intimately tied to the electronic structure of solids; in the visible wavelength regime, it reports on transitions from the valence to conduction band, while in the extreme ultraviolet (XUV) or x-ray regimes, it probes transitions from core states into the conduction band. The current industrial development of XUV lithography at 13.5 nm will eventually require the extension of existing optical metrology techniques into the XUV [2,3]. Such techniques require knowledge of the broadband complex refractive index. Because of the element-specific nature of core-conduction band transitions, XUV absorption and the corresponding complex-valued refractive index provide a wealth of information with high sensitivity to atomic number, spin state, and orbital character [4–6].

Additionally, as attosecond time-resolved measurements in solids become more common [7–9], there is increased interest in studying XUV refractive indices [10–12], as the center frequency of attosecond pulses necessarily lies in the XUV part of the spectrum. These properties make attosecond pulses very attractive for studying element-specific core-to-valence excitations, allowing the tracking of ultrafast oxidation state changes [13] and charge transfer processes [14,15]. Analysis of these measurements relies heavily on high-quality refractive indices in the XUV spectral range, which may not be available because synchrotron studies typically focus on harder x rays.

Germanium (Ge) is a ubiquitous semiconductor with diverse applications ranging from sensors to photovoltaics [16,17]; it has more recently been studied extensively using XUV time-resolved spectroscopies to follow both electrons in the conduction band and holes in the valence band [10,18,19]. In these studies, carrier dynamics were tracked near the Ge $M_{4,5}$ absorption edge from ~28 – 33 eV, and analysis required knowledge of the complex-valued dielectric function in this spectral range. The complex-valued dielectric function of germanium has been retrieved in the visible to near-ultraviolet part of the electromagnetic spectrum through full ellipsometry of reflected light from a Ge surface [20,21], and the results have been related to underlying valence-to-conduction band transitions [22]. Characterization of the dielectric function at higher photon energies up to 25 eV was achieved through combined reflectance and transmittance measurements in combination with a Kramers–Kronig transform [23–25].

The complex refractive index of Ge in the XUV was previously obtained through multi-angle reflection measurements [26] and by Kramers–Kronig analysis of atomic photoabsorption cross sections [27]. Both studies revealed the clear signature of the Ge $M_{4,5}$ edge around 29.5 eV but lacked the energy

resolution required to observe the more detailed structures above the absorption edge. Another study obtained more detailed high-energy structures in the normal incidence reflection spectrum of Ge [28], but it did not retrieve a refractive index for those energies. In this work, we employ multi-angle reflectance measurements to recover the complex-valued refractive index of Ge around the $M_{4,5}$ edge, providing access to the high-energy structures previously observed in Ref [28], giving access to several new structures, and allowing unambiguous assignment of the features present.

2. MATERIALS AND METHODS

Germanium single-crystal wafers of 500 μm thickness, (⟨100⟩ orientation) with surface roughness of less than 1 nm were purchased commercially (University Wafers Inc.) and stored under nitrogen until use. In Ref. [29] it was found that the oxide of Ge grows by less than 1 nm during one day, which minimizes possible surface contamination that could affect the measured refractive index.

The absolute reflectance was characterized at the synchrotron facilities of the Advanced Light Source (ALS) (Beamline 6.3.2) at the Lawrence Berkeley National Laboratory (LBNL) by measuring the reflectance at six different angles of incidence (60, 65, 70, 75, 80, and 85 with respect to the surface normal) for *s*-polarized XUV light.

The reflectivity setup has been described elsewhere [30]. Beamline 6.3.2 uses a variable line spaced plane grating and slit to select wavelengths with a wavelength precision 0.007% and a relative bandwidth of $\Delta\lambda/\lambda = 0.0123\%$. The beam is then focused onto the sample in a 10 μm × 300 μm spot size, and the reflectance is measured with an uncertainty of 0.08% in steps of 0.09 eV. The measured reflectance is shown in Fig. 1. The measured reflectance generally decreases with increasing angle of incidence. Moreover, there is a sharp drop and subsequent rise near 29.5 eV, which has previously been assigned to the Ge $M_{4,5}$ absorption edge attributed to transitions from the spin orbit split $3d_{5/2,3/2}$-core levels to the conduction band.

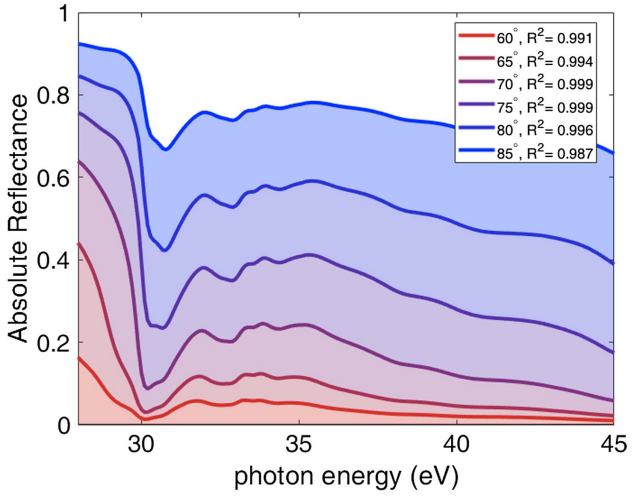

Fig. 1. Experimentally measured reflectance of Ge at 60°, 65°, 70°, 75°, 80°, and 85° from the normal at room temperature. R^2 shows quality of the overall recovery fit for the refractive index based on the data from each angle, obtained using Eq. (1) (see text).

3. RESULTS AND DISCUSSION

A. Recovery of Refractive Index

The complex refractive index $\tilde{n}$ of a material in the XUV is typically written as $\tilde{n}(\omega) = n(\omega) + i\kappa(\omega)$, where $n(\omega)$ is the real part of the refractive index and $\kappa(\omega)$ is the imaginary part. In general, n describes the phase shift of the incident light per cycle, while κ describes the attenuation of the incident light per cycle. The absolute reflectance R_s for *s* polarization is given by the modified Fresnel equation

$$R_s = \left| \frac{\cos\theta_i - \sqrt{\tilde{n}^2 - \sin^2\theta_i}}{\cos\theta_i + \sqrt{\tilde{n}^2 - \sin^2\theta_i}} \right|^2 e^{-\sigma^2 q^2}. \quad (1)$$

Here θ_i is the angle of incidence measured with respect to the surface normal, and $e^{-\sigma^2 q^2}$ is the Debye–Waller factor, which describes the attenuation of the reflected beam due to scattering at an interface with roughness σ for incident light with scattering vector $q = 4\pi \sin\theta_i/\lambda$. [31] Under our conditions, $\sigma = 1$ nm and $e^{-\sigma^2 q^2}$ ranges from 0.9–0.99. Consequently, surface scattering has a fairly small effect on the reflectance.

In order to retrieve the refractive index, a numerical nonlinear least-squares solver is employed to iteratively reconstruct n and κ using Eq. (1) and the reflectance at the six different angles shown in Fig. 1. The quality of the fit, assessed by the coefficients of determination R^2 shown in Fig. 1, is above 0.98, indicating that Eq. (1) can well describe the reflection behavior of the sample. To calculate the uncertainty in the recovered refractive index, the retrieval algorithm used to recover n and κ is applied to $\vec{R}_0 + \vec{\delta R}$, where $\vec{R}_0$ is the set of measured reflectances $\vec{R}_0 = [R(\theta_1), R(\theta_2)\ldots, R(\theta_6)]$, $\vec{\delta R} = [\pm\delta R(\theta_1), \pm\delta R(\theta_2)\ldots, \pm\delta R(\theta_6)]$, and $\delta R(\theta_n)$ is the uncertainty in the reflectance measured at angle θ_n [32,33]. In this work, $\delta R(\theta_n)$ was taken to be 0.08% of $R(\theta_n)$ based on the previously measured error of the beamline [30]. Because each of the six components of $\vec{\delta R}$ can take on two possible values ($\pm\delta R_i$), the recovery algorithm was run $2^6 = 64$ times, once for each possible value of $\vec{\delta R}$. Error bars were taken from the recovered n and κ values maximally displaced from the refractive index associated with $[R(\theta_1), R(\theta_2)\ldots, R(\theta_6)]$. The resulting refractive index and corresponding uncertainty is shown in Fig. 2. The mean errors for n and κ (0.06% and 5.9%, respectively) differ by 2 orders of magnitude, indicating that this procedure is much more accurate for n than κ (see Section 3.B for details). Because of this, the error in n is contained within the width of the line in Fig. 2(b).

The resulting refractive index recovered from the multi-angle fit is shown in Fig. 2, along with reference values obtained from previous studies [26,27]. Overall, the results obtained in this work agree quite well with those obtained by Henke *et al.* [27] and reasonably with the results obtained by Feuerbacher *et al.* [26]. The recovered κ values show a sharp jump at 30 eV, which has been previously assigned, as noted, to the $M_{4,5}$ absorption edge. The subsequent drop in κ above 35 eV is

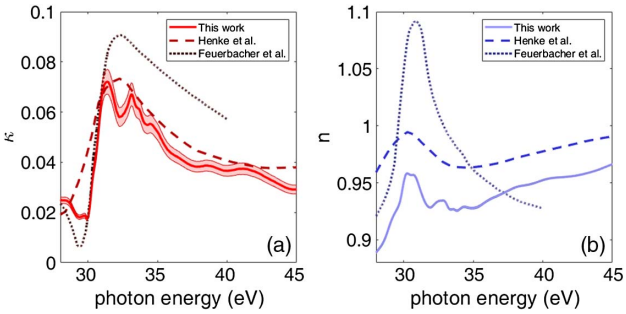

Fig. 2. Retrieved complex refractive index. (a) Retrieved κ (red, solid) compared to previous studies, along with error (red, shaded). (b) Retrieved n (blue, solid), compared to previous studies, along with error (blue, shaded). Because of the small error in n, shaded error bars appear on top of the data.

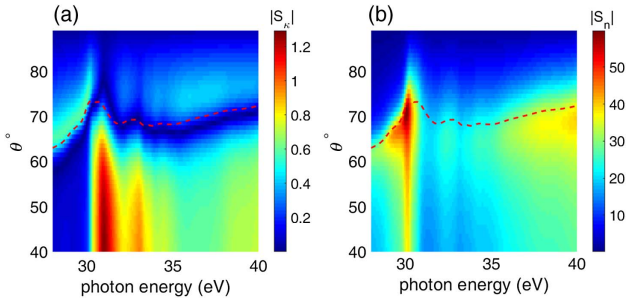

Fig. 3. Sensitivity functions for S_k and S_n. Absolute values of the sensitivity functions (a) S_k and (b) S_n as a function of photon energy and angle of incidence. Estimated critical angle (ϑ_{crit}, red dashed line) traces out the region of low S_k and marks the onset of large S_n.

consistent with core hole effects, which reduce the absorption cross section above the resonance due to scattering of the conduction band wave functions with the core hole created by the XUV photons [34]. Additionally, there is a corresponding dispersive feature in n that is also present in previous work. The recovered n and κ values show the presence of multiple structures between 30 and 45 eV that have not been previously observed in the XUV refractive index. These are discussed in more detail in Section 3.C.

Because κ and n ultimately both report on the same process, namely, polarization of the material by the incident XUV light, κ and n are not independent. As a result, given knowledge of one quantity (n or κ), the other can in theory be found via the Kramers–Kronig relations [35]. Accordingly, comparison of the measured n or κ with the n or κ obtained by the Kramers–Kronig transform provides a useful check for self-consistency of our results. To evaluate the results for self-consistency, we applied the Kramers–Kronig transforms to the κ and n in Fig. 2(a), yielding κ_{KK} and n_{kk}, and computed the mean RMS errors $E_\kappa = \sqrt{(\kappa - \kappa_{KK})^2}$ and $E_n = \sqrt{(n - n_{kk})^2}$, yielding $E_\kappa = 0.027$ and $E_n = 0.021$. For comparison, the same values obtained from Kramers–Kronig analysis of Henke *et al.*'s work were $E_\kappa = 0.021$ and $E_n = 0.005$. Accordingly, our κ and n are reasonably consistent with the Kramers–Kronig relations within expected error.

B. Analysis of Recovery

To analyze the accuracy with which n and κ can be determined from multi-angle reflection data, we define the sensitivity function in the same manner as previous work [10,26] as

$$S_f = (f/R_s)(\partial R_s/\partial f), \tag{2}$$

where R_s is the Fresnel reflectance from Eq. (1) and f stands for n or κ. This function is the ratio of error in reflection to the error in the XUV optical constants, which thus provides an estimation of the sensitivity of the recovered refractive index to changes in the input reflectivity. The corresponding sensitivity functions are shown below in Fig. 3. Because $\kappa \ll n$, we show the relative sensitivity (S_f) instead of absolute sensitivity ($\partial R_s/\partial f$) to highlight the relative sensitivity for these disparate quantities; however, analysis of absolute and relative sensitivity shows the same behavior.

Overall, S_κ [Fig. 3(a)] is at least an order of magnitude less than S_n [Fig. 3(b)], indicating that the reflectivity measurements are much more sensitive to n than κ. This result explains the 2-order-of-magnitude difference in the errors associated with the recovery of n and κ. Generally speaking, $\lim_{\kappa\to 0} S_\kappa = 0$, and therefore we attribute the relatively lower sensitivity of the reflectivity to κ as being due to the low κ value of Ge in this wavelength regime. Interestingly, S_κ shows a local minimum in sensitivity, which varies from 60°–72° across the entire energy region surveyed. The local minimum is extremely close to the XUV critical angle of Ge, which is also 60°–72° in this wavelength regime. Indeed, when $\vartheta_{crit} \cong \sqrt{2(1-n)}$ [36] is plotted along with S_κ and S_n (red dashed line, Fig. 3), it is apparent that for $\theta_i \to \vartheta_{crit}$, $S_\kappa \to 0$. This result can be easily explained by the fact that for $\theta_i \vartheta_{crit}$, an evanescent wave forms, and the incident beam experiences total external reflection. As a result, the natural attenuation of the beam due to the complex phase shift associated with κ becomes less significant compared with the already present attenuation of the evanescent wave. Consequently, this work suggests that accurate determination of κ via multi-angle reflection requires angles of incidence $\theta_i \neq \vartheta_{crit}$. Interestingly, there is a small rise in S_κ for $\theta_i > \vartheta_{crit}$ below the $M_{4,5}$ edge, the origin of which is unknown but may be related to the high-energy tail of deep valence transitions. In contrast, S_n shows no local minimum near ϑ_{crit} and grows substantially with less grazing angles of incidence, indicating that accurate determination of n requires angles of incidence lower than ϑ_{crit}. This analysis reveals that grazing angle reflection may lead to poor determination of n and κ in the XUV due to the possibility of total external reflection, and it indicates that, in this system, measurements near ϑ_{crit} are relatively insensitive to κ.

C. Analysis of Refractive Index

The structures observed in the recovered κ [Fig. 2(a)] are highlighted in Fig. 4(a). Single peaks at 30.3, 31.36, 38.69, and 41.29 eV as well as doublet structures at 33.1/33.67 eV and 34.45/35.12 eV are apparent. Of these structures, those at 31.36, 38.69, and 41.29 eV have not been observed previously.

As previously mentioned, the abrupt rise of κ at 30 eV is due to the onset of the $M_{4,5}$ edge from 3d-core states into unoccupied states in the conduction band. As such, the absence of a

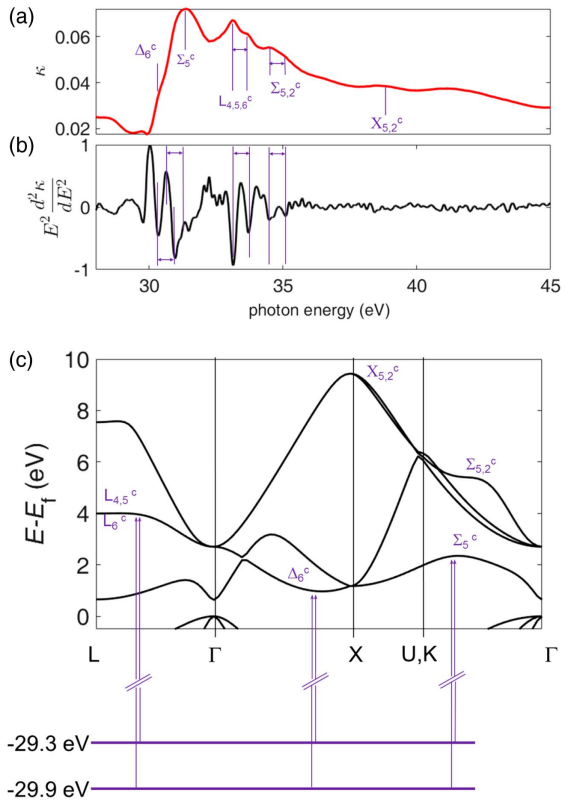

Fig. 4. Recovered κ with assigned transitions in band structure. (a) Recovered κ with specific transitions. (b) Second energy derivative. Vertical bars spaced by 0.6 eV, corresponding to the 0.6 eV spin-orbit splitting of the 3d-core levels. (c) Band structure showing example transitions from 3d-core levels.

peak at 32.4 eV indicates that no significant surface oxidation has occurred, as GeO_2 is known to shift the $M_{4,5}$ edge by 2.4 eV [37]. Because the 3d-core states have an essentially flat dispersion, near the $M_{4,5}$ edge, peaks in κ correspond to regions of the conduction band structure that have both flat dispersion (high joint density of states with respect to the core levels) and high p character (as dictated by angular momentum selection rules for the XUV transition) [10,18].

Because the 3d-core states are spin-orbit split by 0.6 eV, peaks in κ should occur as doublets spaced by 0.6 eV. To analyze the peaks in κ for evidence of doublet structure, the second derivative of κ with respect to energy is shown below in Fig. 4(b) (black). The doublet spacing of 0.6 eV present in the second derivative (black) reveals that the single peaks at 30.3 eV and 31.36 eV in κ are in fact doublets with this splitting. This suggests that the peaks at 30.3 eV and 31.36 eV in κ originate from transitions from the core states into single regions of the conduction band. The peak at 38.69 eV, by contrast, shows no doublet structure within the noise, indicating that it may not originate from a single transition. The lack of a doublet structure in the peak at 38.69 eV could, however, be due to the weak nature of this transition.

In order to assign the features in Fig. 4(a), we use the energies of the peaks and consider angular momentum selection rules along with the results of a band structure adapted from [18], which are shown below in Fig. 4(c). The resulting assignments are summarized in Table 1. The peak at 30.3 eV is assigned to transitions into the mostly p-character Δ_6^c band, as the band structure calculations show this band to be 0.97 eV above the valence band maximum (VBM), which is known to be 29.3 eV above the $3d_{3/2}$-core level, yielding an expected energy of 30.27 eV for this transition. This assignment is similar to structures observed in near-normal incidence reflectance measurements in Ref. [28] but has not previously been observed in the complex refractive index. The peak at 31.36 eV is assigned to the mostly p-character Σ_5^c band, which has a flat region 2.1–2.3 eV above the VBM, giving an expected transition energy of 31.4–31.6 eV with respect to the $3d_{3/2}$-core level. This assignment stands in contrast with previous work on XUV reflectance [26], which was unable to resolve this transition and instead assigned it to a broadened transition at 32 eV. The doublet at 33.1/33.67 eV is assigned to transitions from the spin-orbit split core states into the $L_{4,5,6}^c$ bands, which have high p character and should occur at 4 eV above the VBM (at 33.3 eV with respect to the $3d_{3/2}$-core level). The doublet at 34.67 eV is tentatively assigned to the $\Sigma_{5,2}^c$ band, which occurs at 5.4 eV above the VBM (34.7 eV above the $3d_{3/2}$-core level). The peak at 38.69 eV is assigned to the high p-character $X_{5,2}^c$ band, which is 9.4 eV above the VBM, yielding an expected transition energy of 38.7 eV. Despite having a relatively large density of states, this peak is extremely weak in the recovered κ. The weak peak 41.29 eV roughly matches in energy with higher-lying X bands, which have appreciable p-character density of states between 11.58–12.6 eV above the VBM corresponding to an expected transition energy of 40.88–41.89 eV; however, due to the weak nature of the peak and the imperfect match with any specific band, this transition cannot be unambiguously assigned.

Table 1. Observed Structures in κ and Assignments

Peak Energy (eV)	Band Assignment	% p Character
30.30	Δ_6^c	46
31.36	Σ_5^c	45
33.10	$L_{4,5,6}^c$	76
33.67	$L_{4,5,6}^c$	76
34.45	Σ_5^c	71
35.12	$\Sigma_{5,2}^c$	71
38.69	$X_{5,2}^c$	93

4. CONCLUSION

The high-resolution complex-valued refractive index recovered in this work allows determination and assignment of many structures that have not previously been observed in the refractive index. Further, our work reveals several new structures that have not been observed by any method, and these are assigned to the Σ_5^C and the $X_{5,2}^C$ bands. Finally, our analysis indicates that multi-angle reflection is much more sensitive to n than κ. This issue is in part attributed to total external reflection at the critical angle. Observation and assignment of these features will pave the way for analysis of time-resolved XUV studies in Ge. This work constitutes a substantial improvement on the

previously available refractive index of Ge in the XUV, and it paves the way for future XUV studies of dynamics by transient reflectivity in Ge.

Funding. Army Research Office (ARO) (WN911NF14-1-0383); Swiss National Science Foundation (SNF) (P2EZP2_165252, P300P2_174293); Office of Energy Efficiency and Renewable Energy (EERE); Air Force Office of Scientific Research (AFOSR) (FA9550-15-1-0037); W. M. Keck Foundation; Office of Assistant Secretary of Defense for Research and Engineering; Defense Sciences Office, DARPA (DSO, DARPA) (W31P4Q-13-1-0017).

REFERENCES

1. E. Hecht, *Optics*, 4th ed. (1998).
2. C. Wagner and N. Harned, "EUV lithography: lithography gets extreme," Nat. Photonics **4**, 24–26 (2010).
3. A. J. Den Boef, "Optical wafer metrology sensors for process-robust CD and overlay control in semiconductor device manufacturing," Surf. Topogr. Metrol. Prop. **4**, 023001 (2016).
4. G. Van Der Laan, "$M_{2,3}$ absorption spectroscopy of 3d transition-metal compounds," J. Phys. Condens. Matter **3**, 7443–7454 (1991).
5. R. Qiao, T. Chin, S. J. Harris, S. Yan, and W. Yang, "Spectroscopic fingerprints of valence and spin states in manganese oxides and fluorides," Curr. Appl. Phys. **13**, 544–548 (2013).
6. C. M. Jiang, L. R. Baker, J. M. Lucas, J. Vura-Weis, A. P. Alivisatos, and S. R. Leone, "Characterization of photo-induced charge transfer and hot carrier relaxation pathways in spinel cobalt oxide (Co3O4)," J. Phys. Chem. C **118**, 22774–22784 (2014).
7. H. Mashiko, K. Oguri, T. Yamaguchi, A. Suda, and H. Gotoh, "Petahertz optical drive with wide-bandgap semiconductor," Nat. Phys. **12**, 741–745 (2016).
8. H. Mashiko, Y. Chisuga, I. Katayama, K. Oguri, H. Masuda, J. Takeda, and H. Gotoh, "Multi-petahertz electron interference in Cr:Al_2O_3 solid-state material," Nat. Commun. **9**, 1468 (2018).
9. M. Schultze, K. Ramasesha, C. D. Pemmaraju, S. A. Sato, D. Whitmore, A. Gandman, J. S. Prell, L. J. Borja, D. Prendergast, K. Yabana, D. M. Neumark, and S. R. Leone, "Attosecond band-gap dynamics in silicon," Science **346**, 1348–1352 (2014).
10. C. J. Kaplan, P. M. Kraus, A. D. Ross, M. Zürch, S. K. Cushing, M. F. Jager, H.-T. Chang, E. M. Gullikson, D. M. Neumark, and S. R. Leone, "Femtosecond tracking of carrier relaxation in germanium with extreme ultraviolet transient reflectivity," Phys. Rev. B **97**, 1–9 (2018).
11. A. Cirri, J. Husek, S. Biswas, and L. R. Baker, "Achieving surface sensitivity in ultrafast XUV spectroscopy: $M_{2,3}$-edge reflection-absorption of transition metal oxides," J. Phys. Chem. C **121**, 15861–15869 (2017).
12. J. Husek, A. Cirri, S. Biswas, and L. Robert Baker, "Surface electron dynamics in hematite (α-Fe_2O_3): correlation between ultrafast surface electron trapping and small polaron formation," Chem. Sci. **8**, 8170–8178 (2017).
13. J. Vura-Weis, C. M. Jiang, C. Liu, H. Gao, J. M. Lucas, F. M. F. F. De Groot, P. Yang, A. P. Alivisatos, and S. R. Leone, "Femtosecond $M_{2,3}$-edge spectroscopy of transition-metal oxides: photoinduced oxidation state change in α-Fe_2O_3," J. Phys. Chem. Lett. **4**, 3667–3671 (2013).
14. C.-M. Jiang, L. Robert Baker, J. Matthew Lucas, J. Vura-Weis, A. Paul Alivisatos, and S. R. Leone, "Characterization of photo-induced charge transfer and hot carrier relaxation pathways in spinel cobalt oxide (Co_3O_4)," J. Phys. Chem. C **118**, 22774–22784 (2014).
15. L. R. Baker, C. M. Jiang, S. T. Kelly, J. M. Lucas, J. Vura-Weis, M. K. Gilles, A. P. Alivisatos, and S. R. Leone, "Charge carrier dynamics of photoexcited Co_3O_4 in methanol: extending high harmonic transient absorption spectroscopy to liquid environments," Nano Lett. **14**, 5883–5890 (2014).
16. L. Tang, S. E. Kocabas, S. Latif, A. K. Okyay, D. S. Ly-Gagnon, K. C. Saraswat, and D. A. B. Miller, "Nanometre-scale germanium photodetector enhanced by a near-infrared dipole antenna," Nat. Photonics **2**, 226–229 (2008).
17. N. E. Posthuma, G. Flamand, W. Geens, and J. Poortmans, "Surface passivation for germanium photovoltaic cells," Sol. Energy Mater. Sol. Cells **88**, 37–45 (2005).
18. M. Zürch, H.-T. Chang, L. J. Borja, P. M. Kraus, S. K. Cushing, A. Gandman, C. J. Kaplan, M. H. Oh, J. S. Prell, D. Prendergast, C. D. Pemmaraju, D. M. Neumark, and S. R. Leone, "Direct and simultaneous observation of ultrafast electron and hole dynamics in germanium," Nat. Commun. **8**, 15734 (2017).
19. M. Zürch, H.-T. Chang, P. M. Kraus, S. K. Cushing, L. J. Borja, A. Gandman, C. J. Kaplan, M. H. Oh, J. S. Prell, D. Prendergast, C. D. Pemmaraju, D. M. Neumark, and S. R. Leone, "Ultrafast carrier thermalization and trapping in silicon-germanium alloy probed by extreme ultraviolet transient absorption spectroscopy," Struct. Dyn. **4**, 044029 (2017).
20. D. T. F. Marple and H. Ehrenreich, "Dielectric constant behavior near band edges in CdTe and Ge," Phys. Rev. Lett. **8**, 87–89 (1962).
21. D. E. Aspnes and A. A. Studna, "Dielectric functions and optical parameters of Si, Ge, GaP, GaAs, GaSb, InP, InAs, and InSb from 1.5 to 6.0 eV," Phys. Rev. B **27**, 985–1009 (1983).
22. D. Brust, J. C. Phillips, and F. Bassani, "Critical points and ultraviolet reflectivity of semiconductors," Phys. Rev. Lett. **9**, 94–97 (1962).
23. H. R. Philipp and E. A. Taft, "Optical constants of silicon in the region 1 to 10 ev," Phys. Rev. **120**, 37–38 (1960).
24. O. P. Rustgi, J. S. Nodvik, and G. L. Weissler, "Optical constants of germanium in the region 0-27 ev," Phys. Rev. **122**, 1131–1134 (1961).
25. H. R. Philipp and H. Ehrenreich, "Optical properties of semiconductors," Phys. Rev. **129**, 1550–1560 (1963).
26. B. Feuerbacher, M. Skibowski, R. P. Godwin, and T. Sasaki, "Optical constants of germanium in the region of the $M_{4,5}$ edge," J. Opt. Soc. Am. **58**, 1434–1440 (1968).
27. B. L. Henke, E. M. Gullikson, and J. C. Davis, "X-ray interactions: photoabsorption, scattering, transmission, and reflection at E = 50-30, 000 eV, Z = 1–92," At. Data Nucl. Data Tables **54**, 181–342 (1993).
28. M. Taniguchi, S. Suga, S. Shin, K. Inoue, M. Seki, and H. Kanzaki, "Core-level reflectance spectroscopy of germanium by means of synchrotron radiation," Solid State Commun. **44**, 85–88 (1982).
29. S. K. Sahari, H. Murakami, T. Fujioka, T. Bando, A. Ohta, K. Makihara, S. Higashi, and S. Miyazaki, "Native oxidation growth on Ge(111) and (100) surfaces," Jpn. J. Appl. Phys. **50**, 04DA12 (2011).
30. J. H. Underwood, E. M. Gullikson, M. Koike, P. J. Batson, P. E. Denham, K. D. Franck, R. E. Tackaberry, and W. F. Steele, "Calibration and standards beamline 6.3.2 at the advanced light source," Rev. Sci. Instrum. **67**, 3372 (1996).
31. J. Als-Nielsen and D. McMorrow, *Elements of Modern X-Ray Physics* (Wiley, 2002).
32. C. A. D. Roeser, A. M. T. Kim, J. P. Callan, L. Huang, E. N. Glezer, Y. Siegal, and E. Mazur, "Femtosecond time-resolved dielectric function measurements by dual-angle reflectometry," Rev. Sci. Instrum. **74**, 3413–3422 (2003).
33. T. Shih, M. T. Winkler, T. Voss, and E. Mazur, "Dielectric function dynamics during femtosecond laser excitation of bulk ZnO," Appl. Phys. A **96**, 363–367 (2009).
34. G. D. Mahan, "Optical properties of solids," in *Many-Particle Physics*, 3rd ed. (2000), pp. 579–626.
35. E. Shiles, T. Sasaki, M. Inokuti, and D. Y. Smith, "Self-consistency and sum-rule tests in the Kramers-Kronig analysis of optical data: applications to aluminum," Phys. Rev. B **22**, 1612–1628 (1980).
36. D. Attwood, *Soft X-Rays and Extreme Ultraviolet Radiation: Principles and Applications* (1999).
37. S. K. Sahari, H. Murakami, T. Fujioka, T. Bando, A. Ohta, K. Makihara, S. Higashi, and S. Miyazaki, "Native oxidation growth on Ge(111) and (100) surfaces," Jpn. J. Appl. Phys. **50**, 04DA12 (2011).